Experimental and computational study of unsteady hypersonic cavity flows

S. Creighton and R. Hillier
Department of Aeronautics, Imperial College,
London, UK

ABSTRACT

This paper presents a combined experimental and computational study of annular cavities on a semi-angle cone in a Mach 8·9 flow. A range of cavity length-to-depth ratios has been considered, and a parameter has been determined that distinguishes between 'weak oscillations' and 'strong oscillations' of the cavity flow. Essentially the work identifies the transition from the case where the flow can be regarded as 'pure cavity flow' to that where the flow behaviour is tending towards that of a 'spiked blunt body'. The CFD simulations also suggest that, for a certain range of cavity scale, the limiting cavity flow state depends upon the flow initialisation process; it may be weak or strongly oscillating.

NOMENCLATURE

$\bar{a}$	mean speed of sound in cavity
D_B	depth of cavity back face
D_F	depth of cavity front face
L_C	distance across cavity
L_F	wetted length along fore-body
M	Mach number
P	pressure
S	wetted distance
μ	Mach angle
γ	ratio of specific heats
δ	cone semi-angle
θ	shock wave angle
ρ	density

Subscripts

$( )c$	cavity
$( )_E$	boundary-layer edge conditions
$( )_\infty$	freestream conditions

1.0 INTRODUCTION

Cavity flow combines several mechanisms, including oscillating shear layers, acoustic disturbances and unsteady shock wave propagation. In an early paper Krishnamurty[1] examined subsonic and supersonic rectangular cutouts, with application to weapons bays. He noted a relationship between cavity length and the frequency of unsteady acoustic radiation. Charwat *et al*[2] used the length to depth ratio (L/D) to classify cavity flows.

For geometries with the L/D ratio below approximately 11·5 the flow was classed as 'open cavity flow'. The shear layer, separating from the front lip, bridges the cavity completely.

Geometries with larger L/D ratios were classed as 'closed cavity flow'. The shear layer does not span the cavity but attaches onto the cavity floor, forming a separated region behind the front wall. The shear layer then separates from the cavity floor upstream of the rear wall and passes over the rear lip.

In many of the cavity studies in the literature the attached boundary-layer state upstream of the cavity is not clear, and indeed the laminar-transitional-turbulent state of the free shear layer is often unknown or not commented on. In all the following studies it is

Paper No. 3176. This is an invited paper published to celebrate the 100th anniversary of Imperial College, London.

https://doi.org/10.1017/S0001924000004851 Published online by Cambridge University Press

known that the boundary layer at separation, that is at the upstream lip of the cavity, is very thin compared with the cavity scales (that is, length and depth).

Rossiter[3] identified a shear layer oscillation for rectangular cavities which comprised both random and periodic components. He developed a semi-empirical formula to predict the dominant frequencies of oscillation, which was then improved by the key study of Heller and Bliss[4] who examined a range of cavity L/D ratios for Mach numbers of 0·8 to 2·0. This study also proposed a model of the oscillation mechanism which comprise cycles of 'breathing-in' and 'breathing-out' of mass to and from the cavity. According to this model the oscillation begins with the impingement of a shear layer disturbance – in essence a vortex structure – on the rear lip of the cavity. This provides the mass entrainment mechanism and simultaneously a nearly-plane shock is formed which propagates upstream through the cavity. When this reflects from the front wall of the cavity, the shear layer is 'pushed-up', away from the cavity. The shear layer very shortly 'lifts-off' the rear lip and mass ejection begins. Next the reflected shock moving downstream through the cavity passes through a new upstream propagating wave. The cycle closes when the upstream, reflected, propagating wave reaches the rear wall. The shear layer impinges on to the rear lip and a new internal upstream propagating shockwave is generated.

The above are key experimental studies, but for other early experimental studies see, Nicoll[5], Hahn[6], Sarohia[7], Rockwell and Kinsley[8], Nestler[9,10] and the review paper by Rockwell and Naudascher[11].

The first numerical study, of cavity flow, was conducted by Hankey and Shang[12] in 1980. Using the MacCormack scheme and the Cebeci-Smith eddy viscosity model they examined, in two-dimensions, one of the cases implemented by Heller and Bliss in their experimental study, M = 1·5, L/D = 2·25 with a thin (relative to the cavity scale) turbulent boundary layer at separation. Reasonable agreement was found between the experimental and numerical data sets.

Dusing *et al*[13] presented a combined experimental-numerical study of supersonic cavity flow. Using the thin-layer Navier-Stokes equations for a freestream flow of M = 2·0, L/D = 2·0 they found good agreement with experimental results. Their results also indicated the shear layer oscillation mechanism was more complex than first established by Heller and Bliss and others. Similar conclusions were found by[14,15,16].

Morgenstern and Chokani published several studies[17,18,19] for both two-dimensional and three-dimensional cavity simulations providing good agreement with experiment. Colonius *et al*[20] using direct numerical simulation (DNS) for low Reynolds number, cavity flows found that the shear layer was well characterised by Rossiter modes.

At hypersonic speeds examples of cavity flow tend to feature at small scales, such as the gaps between insulation tiles. One example, with specific application to scram-jet technology, is the use of a cavity as a trapped vortex combustor (TVC)[21,22]. A cavity is used to provide a point for fuel injection and allow for mixing with the free stream. Cavities used in this application often deviate from the generic rectangular cavity shape common to the research literature. Some scram-jet designs incorporate a cavity into the conical compression ram where a rectangular cavity design would not be ideal[22]. There are few research efforts involving non-rectangular cavities, though Edwards *et al*'s study[23] is one good example. They studied the effect of the trailing edge geometry on the flow oscillation, using a Reynolds Averaged Navier-Stokes (RANS) flow solver. For a free stream Mach number of M = 1·5, with cavity L/D = 3·0, it was found that with a cavity trailing end of either a wedge or a curved ramp the level of oscillation was reduced.

The objective of this study is to investigate, experimentally and computationally, the flow field for annular cavities on the surface of a sharp cone. This provides a configuration that, in principle, can produce an axisymmetric time-average flow, even though the unsteady flow field might itself be three-dimensional. There are several other cavity studies in the literature using bodies of revolution with annular cavities. Jackson *et al*[24] used a hollow body of revolution at a Mach number of 9·0, with an annular cavity on a cylindrical segment. This provided open cavity flow. The boundary layer at separation was laminar – and very thin compared with cavity length and depth scales – and, possibly except for the longest cavities, the cavity flow itself was laminar. A similar annular cavity configuration, using a cylindrical after-body, was studied by Hahn[6]. Again the boundary layer at separation was very thin compared with cavity scales, although in this case the studies ranged from laminar to transitional free shear layers. Annular open cavity flows on cones have been used by Nicoll[5], for a basic 10 degrees semi-angle cone at Mach 11, and for a 10 degree semi-angle cone at Mach 8 by Bellone and Stollery[25]. Again, the boundary layer at separation was very thin in both cases. Nicoll[5] reported that the cavity flow was only unsteady once the free shear layer became transitional. Bellone and Stollery[25] report 'only mild unsteadiness'; the fore-cone boundary layer was assumed to be laminar.

2.0 EXPERIMENTAL SETUP

2.1 Gun tunnel facility

The experimental work was conducted in the Imperial College Gun Tunnel. This is a short-duration test facility, operating with nitrogen gas and with a steady run time of approximately 4-6ms and a nominal Mach number of 9·0. The tunnel has three calibrated operating conditions. Table 1. details the 'low' Reynolds number operating condition used for the present study. The intention was to provide, as best as possible, a fully laminar interaction, certainly a flow that is laminar at separation, although maintaining a laminar separated free shear layer may be more problematic. Not only is this an interesting case in its own right but, as part of a general strategy of integrating CFD and experiment, laminar interactions provide a well-defined start point for CFD investigations. It is the intention to use later studies to explore turbulent interactions.

2.2 Model design and instrumentation

The basic model is a 15° semi-angle cone, with a modular construction as shown in Fig. 1. A similar configuration has been used by Bellone and Stollery[25]. Each of the four numbered modules fits onto a central sting (radius R_O = 10mm) but can be removed individually to create various length cavities. The sting provided the cavity floor, but cylindrical collars (radius R_O = 12·94, 16 and 24·43mm) could also be fitted over this sting to reduce the cavity depth for any given length. The wetted (i.e. along the slope) length of each module is 50mm. The cavity created by the removal of module # was simply called cavity #. For example removing both modules 2 and 3 created cavity 23, with a length (L_C) of 100mm between the front and rear lips. Figure 2 provides a schematic for the cone-cavity model, together with the notation.

The instrumentation used in the model was also modular. Pressure transducers, or heat transfer gauges, were mounted into 10mm diameter brass plugs which could be installed into the rear face of cavities 1 through to 4. A limited range of tapping locations was provided and Table 2. lists the positions that were used specifically to record the pressure time-histories that are presented later. Note that each pressure tapping has an 'opposite' with the same radial position, at 180 degrees in azimuth, which allowed the axisymmetry of the flow to be assessed. Kulite miniature pressure transducers were used, positioned just below the wetted surface at the end of short tappings to

https://doi.org/10.1017/S0001924000004851 Published online by Cambridge University Press

Table 1
Test section flow conditions for 'low' Reynolds Number operation

M_∞	$P0_\infty(bar)$	$T0_\infty(K)$	$T_{wall}(K)$	$Re_\infty(/metre)$
8·9(±0·5%)	98(±2%)	1,000(±4%)	293(±2%)	9,540,000(±6%)

minimise response times. The reason why the pressure transducers were not flush-mounted was to avoid any accidental damage to them from the impact of high speed microscopic particles. The recessed arrangement radically reduces the frequency and amplitude response, however, as shown by the time-histories in Fig. 3, where four different tapping diameters (0·6mm, 0·9mm, 1·5mm and 2·5mm) are used to record pressure time-histories on the back-face of cavity 1. It should be noted that since the measurements for the different tapping diameters were made in different runs the time-histories are not synchronised, although the run conditions are identical in each case. The time scale is normalised by the boundary-layer edge velocity U_E (to be presented later) and the cavity length L_C. The individual symbols on the traces indicate the 125kHz sample rate and one sample interval of 0·008ms corresponds approximately to 0·21in TU_E/L_C. This cavity case presents one of the most vigorous unsteady cases and there is a clear discrepancy in recorded fluctuation levels between the different tapping sizes. Figure 4 shows the variation of measured mean pressure and rms fluctuating pressure with tapping diameter for this transducer location (taken from a larger ensemble of data than the short record shown in Fig. 3). The mean is resolved well for all tapping diameters ≥ 0·5mm, but the rms shows significant variations with diameter and it is evident that even the best response, with the largest tapping diameter, fails to capture all the signal energy. Inspection of the highest frequencies present for this largest diameter case (effectively the small 'spikes' superimposed upon the main signal) would indicate that it probably resolves fluctuations up to 10 – 20kHz. The rms trend then indicates the presence of significant fluctuation energy above the 10 – 20kHz range, an observation supported by the CFD modelling of time-histories to be presented later. It is pointless to increase the tapping diameter further, it would exceed that of the transducer itself, and anyway the signal response then moves into a trade-off between frequency resolution and worsening spatial resolution. All later measured data refer specifically to the largest tapping size. Interpretation of the pressure time-histories will focus upon the larger scale, and hence lower frequency, fluctuations which are reasonably well captured by the transducer response; these, in the event, are found to be the most important unsteady events for the highly oscillatory cavity flow cases.

The heat transfer sensors were thin-film platinum resistance-gauges, hand-painted onto machinable ceramic MACOR. Three heat transfer sensors were mounted on the instrumentation plug, and Table 2 specifies the location for the one used specifically to produce time-history data. Gauge output, in the form of temperature time-histories, was reduced digitally to heat transfer histories using the method of Cook and Felderman[26,27]. Heat transfer gauges provide a very high frequency response, but data here have been low-pass filtered at 45kHz as an anti-aliasing measure. This frequency limit is satisfactory for the pressure data which focuses on the larger scale, lower frequency motions. Figure 5 shows measured heat transfer rates (in W/cm^2) on the back face of cavity 1.

Schlieren flow field visualisation used a spark light source, with a flash duration of order 0·1μs. At the tunnel flow speed, even the fastest disturbances would move only of order 0·2mm, which is comparable to the focus resolution of the system. Only one photograph is taken for each firing of the tunnel. Later in the paper a sequence of schlieren photographs is presented for a complete 'shedding cycle'. This has been constructed from a set of individual tests; the placing of the photographs 'in sequence' was assisted by the CFD modelling.

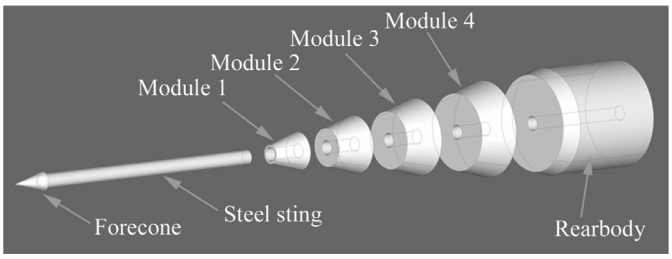


Figure 1. Exploded view of the model.

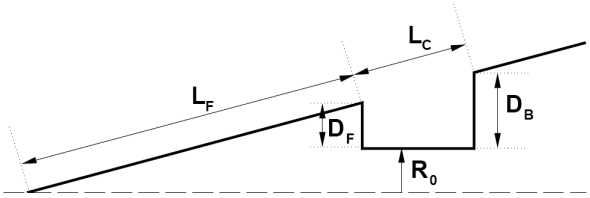


Figure 2. Schematic for the cone-cavity model. L_F and L_C are the wetted distance, from the cone apex to the leading edge of the cavity, and the distance across the cavity respectively. D_F and D_B are the front and back cavity depths and R_0 is the radial distance of the cavity floor from the axis of symmetry.

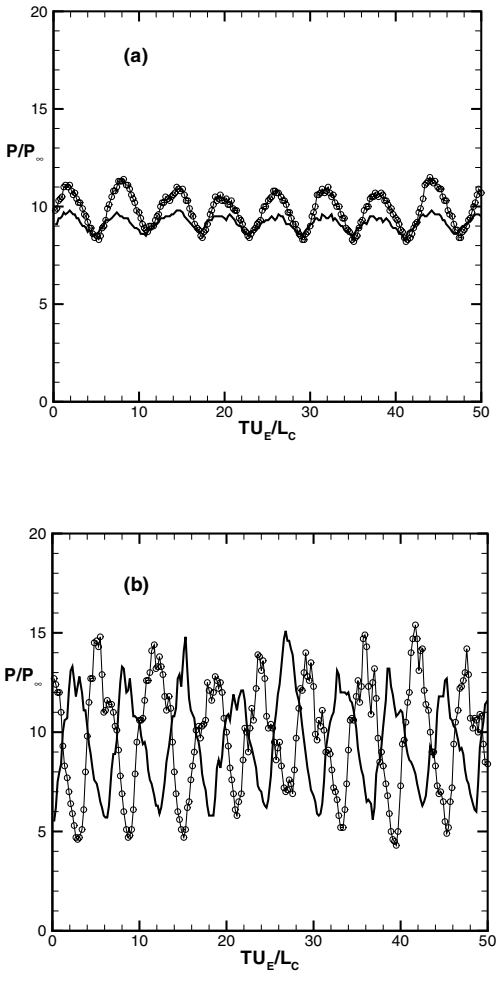


Figure 3. Assessment of frequency response, for four different pressure tapping diameters, using time-history measurements for the cavity L_C/L_F = 1 on the back-face of the cavity 1. Tapping diameters; (a) 0·6mm, solid line ; 0·9mm, solid line plus circles ; (b) 1·5mm, solid line ; 2·5mm, solid line plus circles.

https://doi.org/10.1017/S0001924000004851 Published online by Cambridge University Press

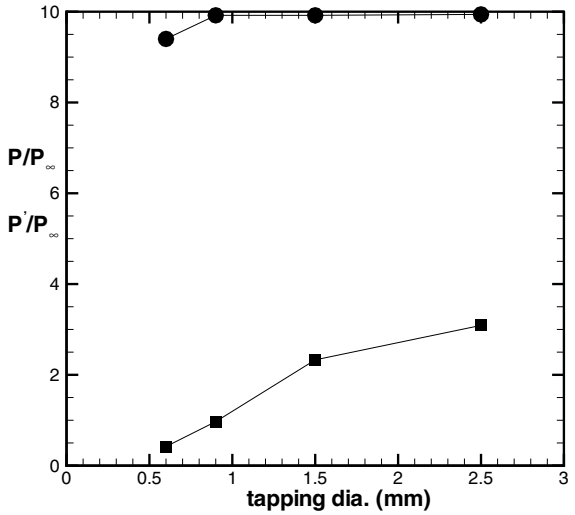


Figure 4. Assessment of frequency response, showing the variation of mean and rms pressures with tapping diameter. Mean pressure, circles; rms pressure, squares.

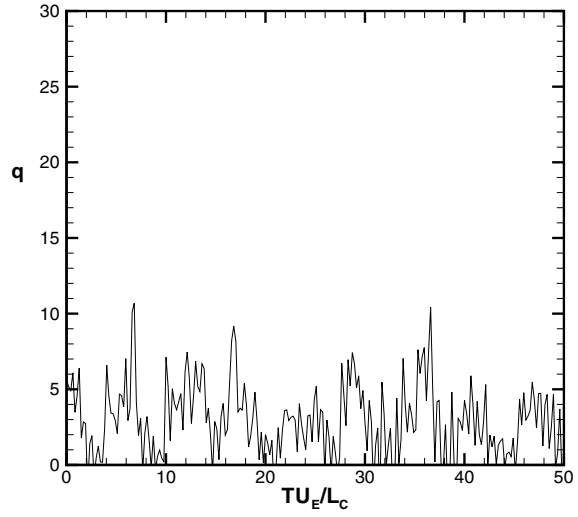


Figure 5. Experimental heat transfer (in W/cm^2) time-history on the back-face of cavity 1.

Table 2
Location of pressure tappings, and heat transfer gauges, used for the time-history data. In each case the location is on the back face of the cavity, measured from the upper rear lip of the cavity. For the pressure measurements the position corresponds to those for a matching pair of transducers separated by 180 degrees in azimuth

cavity	1	2	12	3
pressure	7·5mm	14mm	14mm	15·5mm
heat transfer	11mm	–	–	–

3.0 COMPUTATIONAL MODELLING

3.1 Numerical method

CFD modelling used an axisymmetric second-order-accurate laminar Navier Stokes code. It is hoped that the justification for 'laminar' and 'axisymmetric' will become apparent from the later discussion. Certainly 3D turbulent simulations would have been too ambitious for the range of cases that we wished to survey here. Most details of the method are available elsewhere[24,28], so that only the main points are repeated here. It uses 'convection-diffusion' splitting, solving the convective (i.e. Euler) terms with an explicit second-order upwind Godunov-type solver based on the generalised Riemann problem of Ben-Artzi and Falcovitz[29], and evaluating the full diffusive (viscous) terms with centered differencing and Runga-Kutta time integration. An ideal equation of state for nitrogen (the experimental test gas) is used, together with the following formulation due to Keyes[30] for the temperature dependence of the molecular viscosity (in Kg/m/s).

$$\mu = \frac{1\cdot 418\times 10^{-6} T^{1/2}}{1+116\cdot 4T^{-1}10^{-5/T}} \qquad \ldots (1)$$

Isothermal wall conditions were used, with the wall temperature fixed at the value given in Table 1.

The simulations presented later refer to two types of flow initialisation. One, the 'impulsive start', initialises conditions around the model at the pre-firing (near vacuum) conditions in the test section and with the upstream inflow boundary (just forward of the cone apex) fixed at the steady state tunnel conditions of Table 1. The computation is then marched until a stationary state is achieved. This procedure models some aspects of the true transient start-up of a short duration facility, although the free stream flow establishment time in the CFD is at least one order of magnitude faster than the progressive nozzle-and-test-section flow development found experimentally. Other cases use a 'mapping' process. This was mainly employed when a cavity was elongated, or shortened, slightly, for fixed fore-body length. In this case the initial conditions for the 'new' cavity were mapped from a linear stretching of the 'old' cavity solution. The main reason for this will be explained later, but was essentially used in an assessment of possible dual-states for the cavity flow.

3.2 Mesh and convergence considerations

A structured mesh of quadrilateral cells was employed as illustrated in Fig. 6, with cell refinement adjacent to all solid surfaces to resolve the viscous layers on the fore-/after-bodies as well as in the cavity interior.

Assessing mesh convergence for unsteady flows is difficult, especially since a range of cavity L_C/L_F values has been used. As commented for the resolution of experimental data, cavity 1 represents a significant case because of the large amplitudes of motion. Thus Fig. 7 shows the time-varying pressure computed on the back face of cavity 1, at the same location used for Fig. 3, for the coarse mesh of Fig. 6 (with 100 by 100 cells in the cavity) and two successive refinements, each of which successively halved the cell size in both directions. The signal clearly has a periodic nature, but with an amplitude modulation so that direct comparison of the traces is not precise. It is clear that there is a progressive increase in the extreme positive-going pressure fluctuations as the mesh is refined, although these are so narrow that their contribution to the overall mean is likely to be modest.

Figure 8 presents mean and rms pressure predictions, for the three mesh levels, over the whole wetted length of the cone-cavity-afterbody configuration. The variable S^* is the wetted length, starting on the fore-cone and following a path through the cavity, but

https://doi.org/10.1017/S0001924000004851 Published online by Cambridge University Press

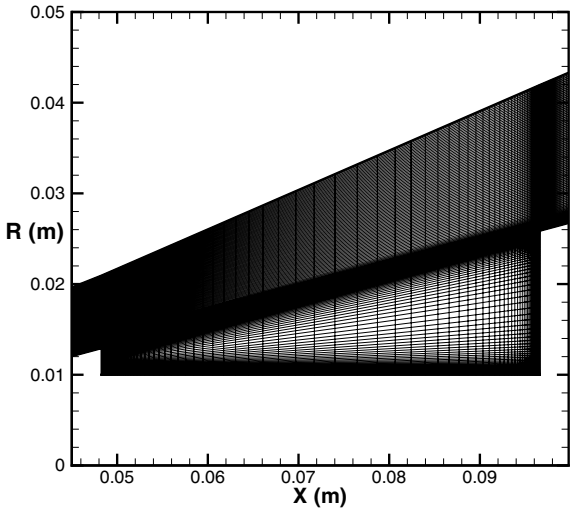


Figure 6. Coarsest mesh for cavity 1 simulation, with 100 by 100 cells in the cavity.

assigning unit length to each segment of the path; thus the model apex is '0', the front and rear upper lips of the cavity are '1' and '4' respectively, the lower corners for the front and rear cavity faces are '2' and '3' respectively and the model trailing edge is '5'. Agreement between the three levels of mesh is generally good, for both mean pressure and rms pressure fluctuations and also agrees well with the measured values of time-averaged pressure on the cavity back face which are also included. The CFD overpredicts the experimental value for the rms pressure. This is attributable to the frequency response characteristics referred to earlier, since the transducer would be unable to resolve the very high frequency events – the 'spikes' – shown in Fig. 7(c). This can also be judged by comparing the CFD of Fig. 7 with the experiment of Fig. 3. The sense of the discrepancy, that is laminar CFD exceeding experimental values, certainly provides some support for the assumption that the flow is laminar rather than turbulent. The main regions of (modest) disagreement between the meshes in Fig. 8 are for $1 \le S^* \le 2$, that is the front face of the cavity (though its true length is very short as shown by Fig. 6), and for the cavity-floor/back-face junction, $S^* = 3$. The shear layer impingement zone straddling the rear lip, at $S^* = 4$, is modelled well at all mesh levels, despite the very large values and flow gradients that appear.

Heat transfer is potentially a better overall measure of mesh-dependence, since it depends more critically than does pressure upon the resolution with time of the boundary layer on the cavity walls and floor. The computed heat transfer time-history in Fig. 9 is for the same cavity case as measured experimentally in Fig. 5. Figure 10 provides an overall surface mesh convergence assessment and includes specific experimental data for the fore-body and the cavity back-face. On the fore-body there is a perfect collapse of the CFD up to approximately $S^* = 0{\cdot}6$, which is the rearmost location of fully attached flow on the fore-body and downstream of this position the predicted separation front intermittently penetrates upstream of the front cavity lip. The presence of this intermittent separation zone on the fore-body is seen best in the CFD by the non-zero values for rms pressure or heat transfer in the region $0{\cdot}6 \le S^* \le 1$. Downstream of $S^* = 0{\cdot}6$ agreement between the different meshes is still generally good, and there is close agreement on the fore-body with the measured data. The main region of discrepancy between the various meshes is on the cavity floor, $2 \le S^* \le 3$, and a discrepancy is evident between CFD and experiment (for the time-average values) on the cavity back-face, $3 \le S^* \le 4$, although the CFD shows very good collapse between the various meshes. The largest

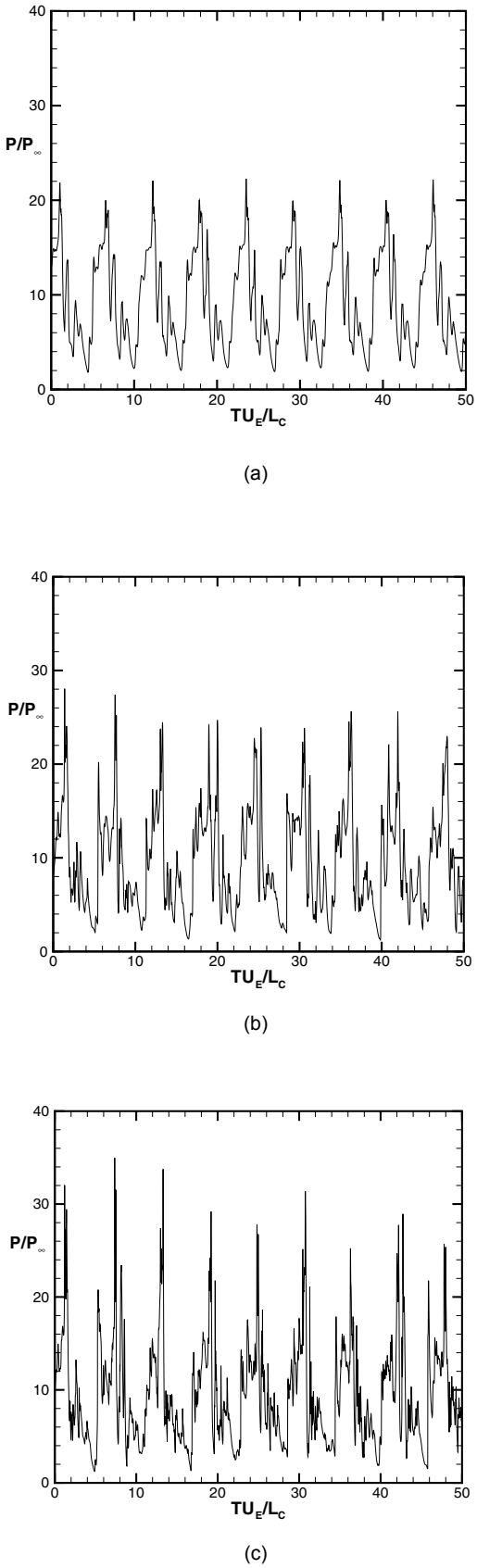
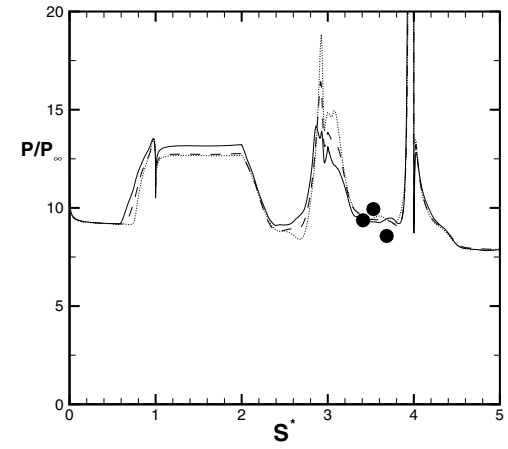
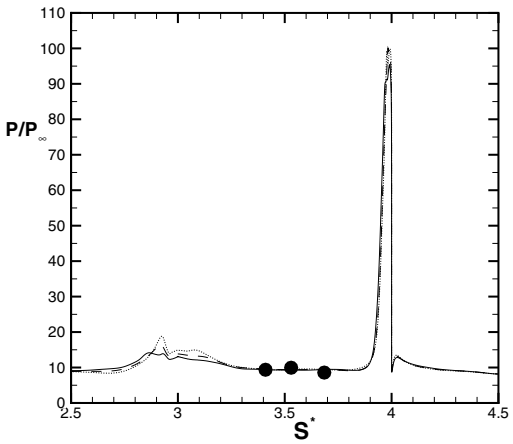


Figure 7. CFD pressure time-histories on the back-face of cavity 1 for three levels of mesh refinement. (a) 100 by 100 cells in the cavity, (b) 200 by 200 cells and (c) 400 by 400 cells.

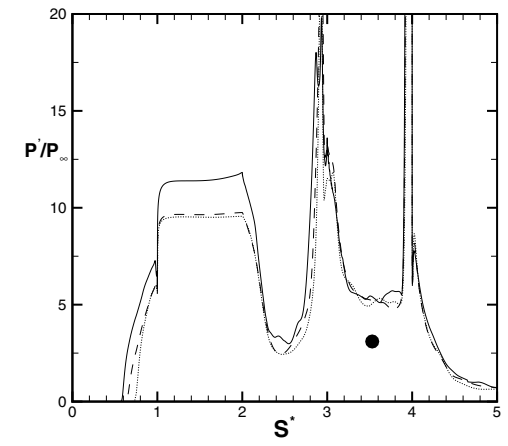
https://doi.org/10.1017/S0001924000004851 Published online by Cambridge University Press



(a)

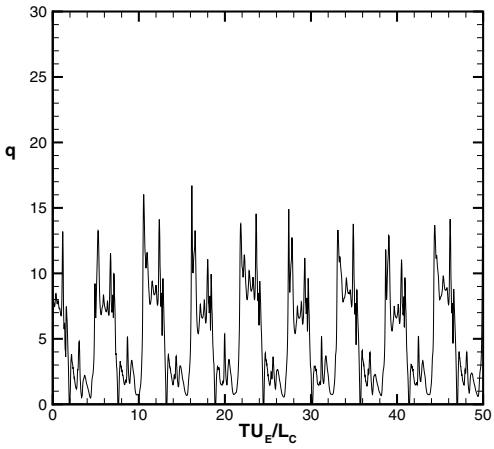


(b)

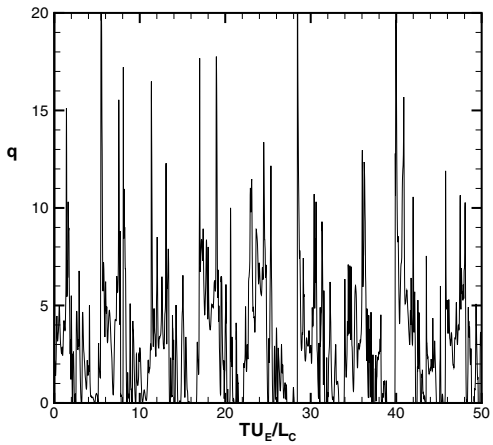


(c)

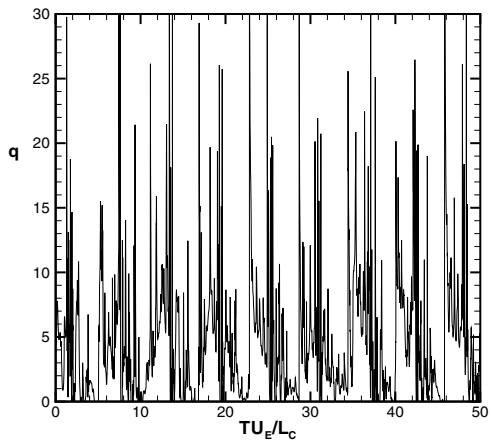
Figure 8. CFD modelling of surface pressure distribution for Cavity 1 for three levels of mesh refinement. 100 by 100 mesh, ...; 200 by 200 mesh, -----; 400 by 400 mesh, ——. The solid symbol represents experimental time-mean data. (a) time-averaged pressure for full length of model, (b) detail for time-averaged pressure in the vicinity of the rear face of the cavity, (c) rms pressure for full length of the model.



(a)



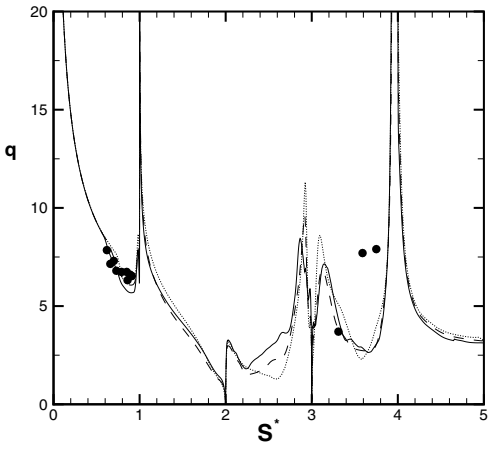
(b)



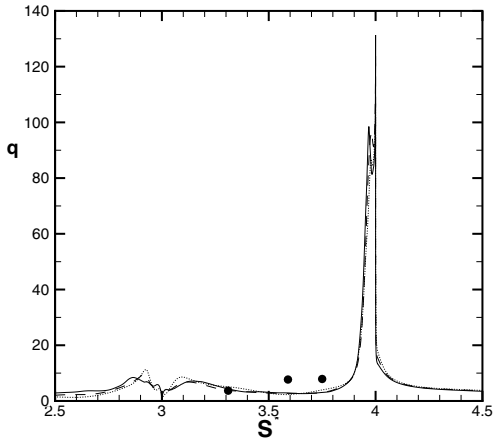
(c)

Figure 9. CFD heat transfer time-histories on the back-face of cavity L_C/L_F = 1 at 11mm from the cavity lip for three levels of mesh refinement. (a) 100 by 100 cells in the cavity, (b) 200 by 200 cells and (c) 400 by 400 cells.

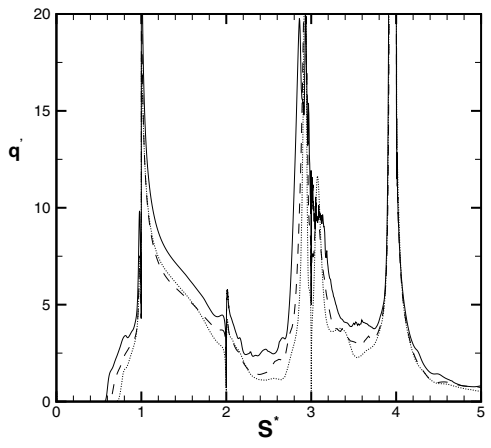
https://doi.org/10.1017/S0001924000004851 Published online by Cambridge University Press



(a)

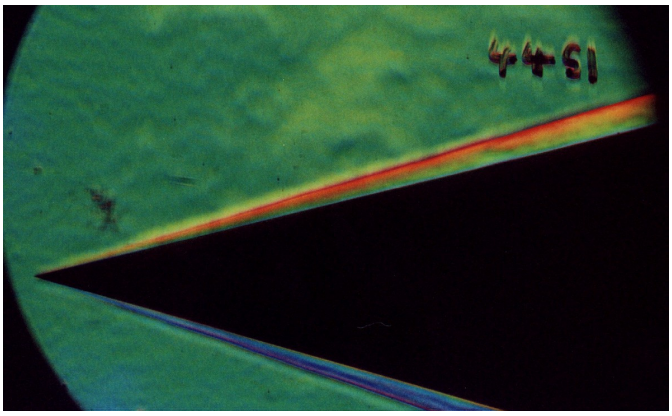


(b)

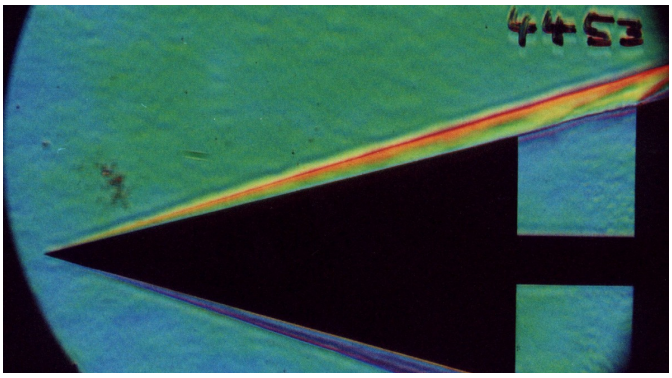


(c)

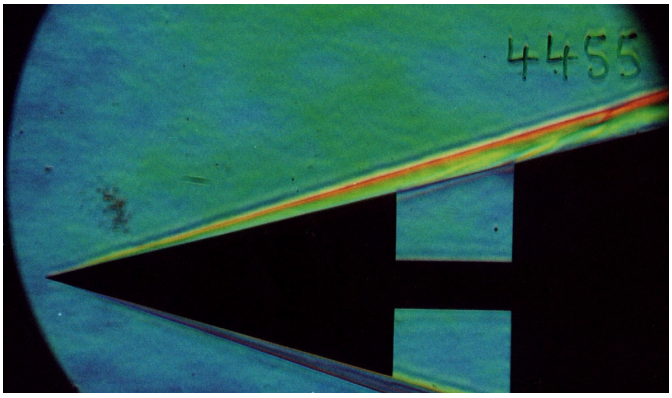
Figure 10. CFD modelling of surface heat transfer for Cavity 1 for three levels of mesh refinement. Legend as for Fig. 8. (a) time-averaged heat transfer (b) detail for time-averaged heat transfer (c) rms heat transfer.



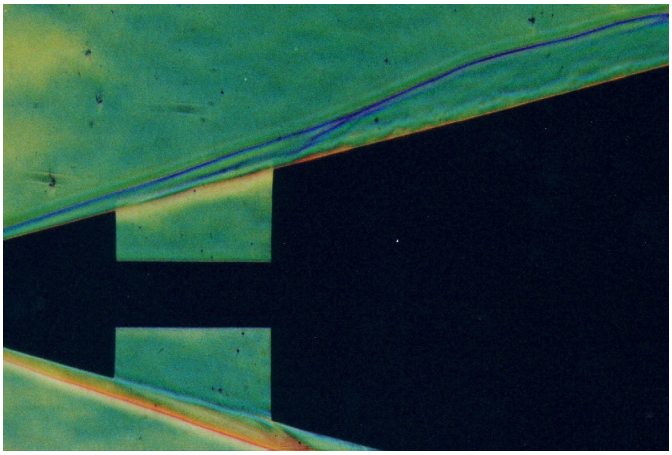
(a)



(b)



(c)



(c)

Figure 11. Schlieren images, top-to-bottom, for the solid cone and cavities 4, 3 and 2 respectively.

https://doi.org/10.1017/S0001924000004851 Published online by Cambridge University Press

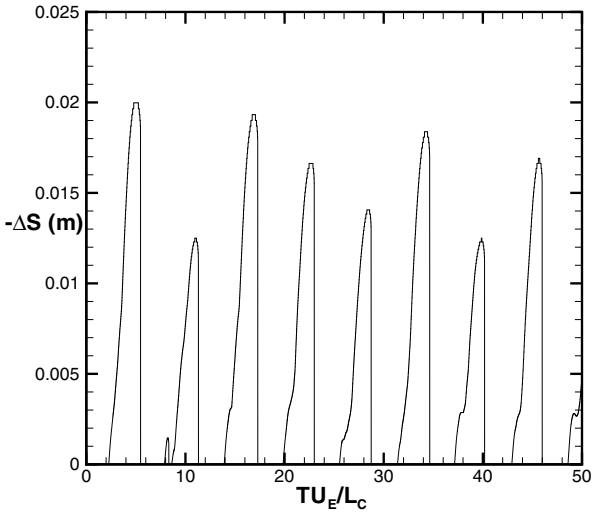


Figure 12. CFD modelling, at finest level of mesh refinement, for cavity 1 for the intermittent movement of the separation position ΔS forwards onto the conical fore-body. The start time of the sequence is arbitrarily set to zero, at a stage in the computation when the fluctuation process appeared to have reached a stationary state.

experiment/CFD discrepancy in the mean value is a CFD underprediction by a factor of more than 2. For a time-averaged quantity this does not relate to frequency response. There is no way to assess whether of not this indicates the appearance of turbulent flow on the cavity back-face (which in turn would have been convected from the reattaching shear layer). An equally strong contender would be the appearance of cross-flows – non-axisymmtric flow – since only weak cross-flows would be required to make significant changes in regions where the basic 2D velocity components are themselves small.

4.0 INITIAL CHARACTERISATION OF THE FLOW FIELD

4.1 Fore-body boundary-layer development

From the CFD the predicted laminar boundary-layer edge conditions for attached flow on the cone fore-body are a Mach number of 5·47 – 5·49, depending upon chordwise position, and a unit Reynolds number of 14·7 million per metre, as given in Table 3. The shortest fore-body (wetted) length of 50mm is the appropriate value for all cases that include cavity 1; the largest fore-body length is for cavity case 4, that is the fore-cone plus modules 1, 2 and 3 in place, which gives a wetted fore-body length of 200mm or a Reynolds number based upon edge conditions of about 2·94 million. Extensive studies have been performed on a variety of axisymmetric geometries in the Imperial College Gun tunnel including sharp and blunted cones (5° semi-angle)[31] and various fore-body configurations leading to cylindrical section after-bodies (e.g. (24) and (32)). These have all been shown to provide laminar boundary-layers for development lengths (and wetted distance Reynolds numbers) beyond those used here. There seems little doubt that the fore-body flow will be laminar up to the separation lip of the cavity for all cases. Table 3. also includes the CFD predictions for laminar boundary-layer displacement and momentum thicknesses, δ_1 and δ_2, immediately upstream of the possible positions for the front lip of the cavity, using (see, for example, Fernholz and Finley[33]):

$$\delta_1 + \frac{\delta_1^{\,2}}{2R_C} = \int_0^{\delta_e} \left(1 - \frac{\rho U}{\rho_e U_e}\right)\left(1 + \frac{y}{R_C}\right) \mathrm{d}y \qquad \ldots (2)$$

$$\delta_2 + \frac{\delta_2^{\,2}}{2R_C} = \int_0^{\delta_e} \frac{\rho U}{\rho_e U_e}\left(1 - \frac{U}{U_e}\right)\left(1 + \frac{y}{R_C}\right) dy \qquad \ldots (3)$$

Here δ_e is the boundary-layer edge thickness, determined by inspection of the computed profiles, and R_C is the local radius of the cone. It should be noted that for the strongly oscillatory cavity cases, the separation position moves, intermittently, forwards of the upstream cavity lip onto the fore-body. The Table 3 values are for the reference case of fully attached boundary layer flow up to the appropriate position for the front lip of the cavity.

4.2 Schlieren visualisation

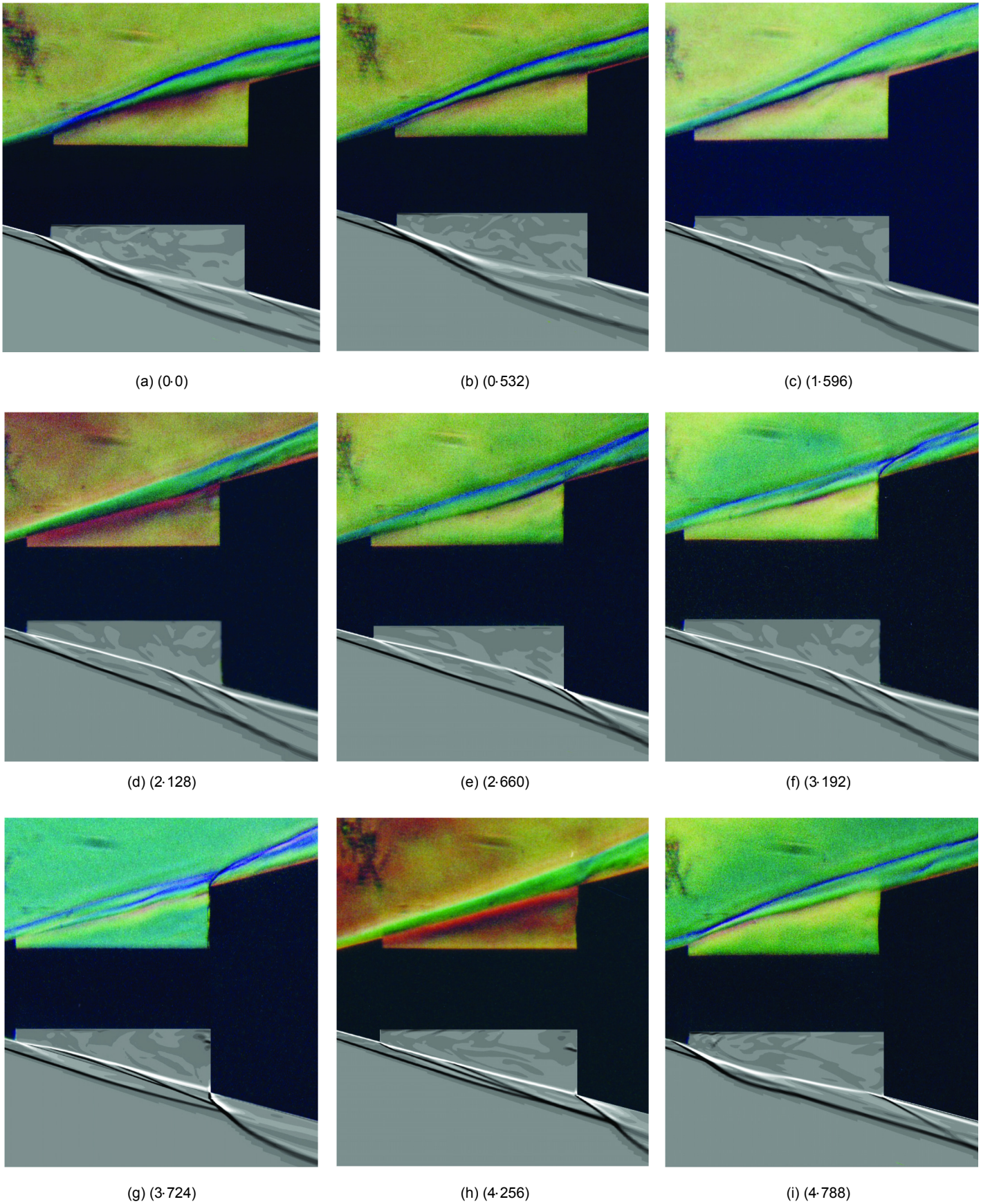
Figure 11. shows schlieren visualisation for the full solid cone model and for cavities 4, 3 and 2 respectively. The boundary layer is so thin that it is only properly visible once it separates at the upstream lip of the cavity. The resultant free shear layer shows every indication of laminar flow, with barely any change in thickness over the cavity length. The only evidence of disturbance in the shear layer is for cavity 2, where slight undulations appear with stream-wise scales that are very large compared to the shear layer thickness and which must be driven by larger scale internal motions within the cavity.

Cavity 1, however, generates a much more significant unsteadiness, which involves both the shear layer and also the shock wave from the cone apex, coupled with the separation position intermittently moving upstream of the front cavity lip along the fore-body. This is demonstrated by Fig. 12 which shows the CFD prediction of the movement of the unsteady separation position on the fore-body, and by the extended sequence of Fig. 13 which shows nine separate experimental visualisations together with comparative CFD. The CFD was accumulated through one full shedding cycle with values given on the figure for TU_e/L_C, where U_e is the computed boundary-layer edge velocity and the cycle starts arbitrarily at $T = 0$. Only one schlieren photograph could be recorded from any given experimental run, however. The schlieren photographs were then chosen, from a large number, as those that best matched the image from the appropriate point in the CFD cycle. Clearly this is a specific selection process, but it does indicate that the scale of excursion of the shear layer, as found experimentally, matches well the range determined from the CFD.

Table 3
Predicted laminar boundary layer properties on the conical fore-body, just upstream of the cavity for the various cavity positions. M_E and Re_E are the boundary layer edge Mach number and unit Reynolds number respectively

s(mm)	M_E	U_E/U_∞	δ1(mm)	δ2(mm)	$Re_E(m^{-1})$	$Re_{\delta 1,E}$	$Re_{\delta 2,E}$
50	5·47	0·956	0·223	0·0209	14,700,000	3,270	306
100	5·48	0·957	0·316	0·0294	14,700,000	4,658	433
150	5·49	0·957	0·387	0·0361	14,700,000	5,682	530
200	5·49	0·957	0·450	0·0415	14,700,000	6,625	612

https://doi.org/10.1017/S0001924000004851 Published online by Cambridge University Press



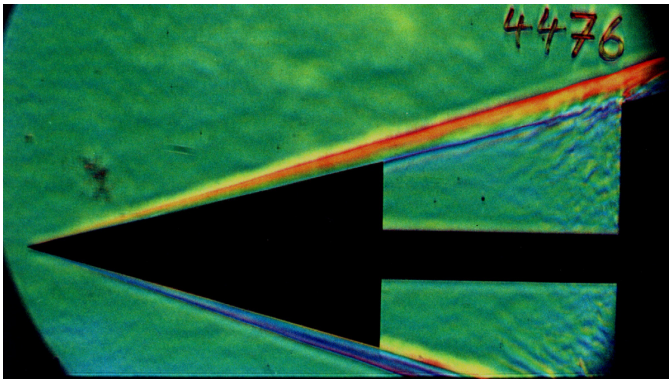
(a) (0·0) (b) (0·532) (c) (1·596)

(d) (2·128) (e) (2·660) (f) (3·192)

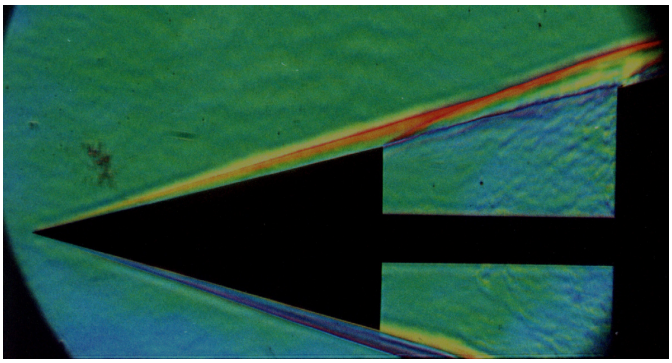
(g) (3·724) (h) (4·256) (i) (4·788)

Figure 13. Schlieren comparison with CFD images for the cavity 1 geometry. Each sub-figure shows the experimental image on the upper half and the numerical on the lower. The dimensionless time TU_E/L_C (in parentheses) shows when the numerical image was captured, with the start of the cycle set arbitrarily to zero.

https://doi.org/10.1017/S0001924000004851 Published online by Cambridge University Press

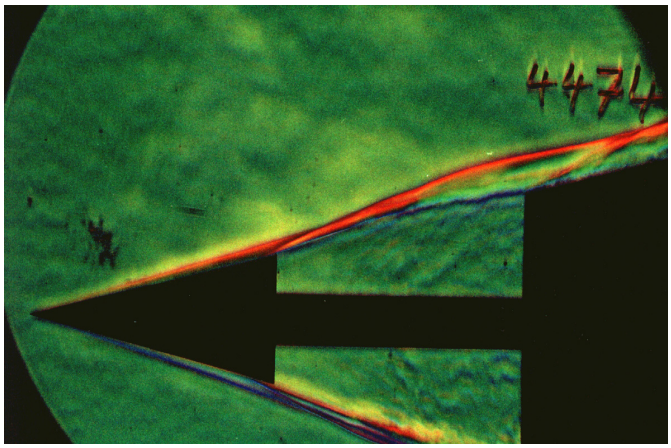


(a)

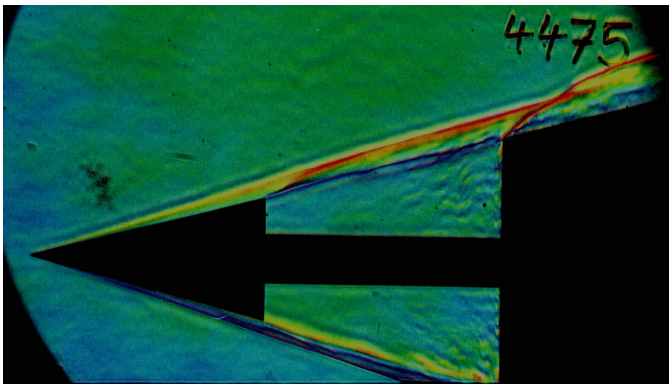


(b)

Figure 14. Schlieren images for the cavity 34 case.



(a)



(b)

Figure 15. Schlieren images for the cavity 23 case.

The sequence of Figs 14, 15 and 16 now shows the double length cavity, L_C = 100mm, for fore-body lengths, L_F , of 150mm, 100mm and 50mm respectively. The most rearward cavity, case 34, shows a nearly straight trajectory for the shear layer with disturbances (with wavelengths of order several shear layer thicknesses) developing in the latter part of its length. The 'side views' show a marked three-dimensionality to these disturbances. The second image of Fig. 14 reveals a clear separation shock wave at the forward cavity lip, indicating a significant local instantaneous pressurisation of the cavity.

For cavity 23 (Fig. 15) a larger scale amplitude motion of the shear layer becomes apparent and these motions now interact with an unsteady motion of both the apex and separation shock waves. Cavity 12 (Fig. 16) shows very large amplitude unsteadiness, with the separation position penetrating instantaneously upstream of the forward lip of the cavity for at least a third of the fore-body length.

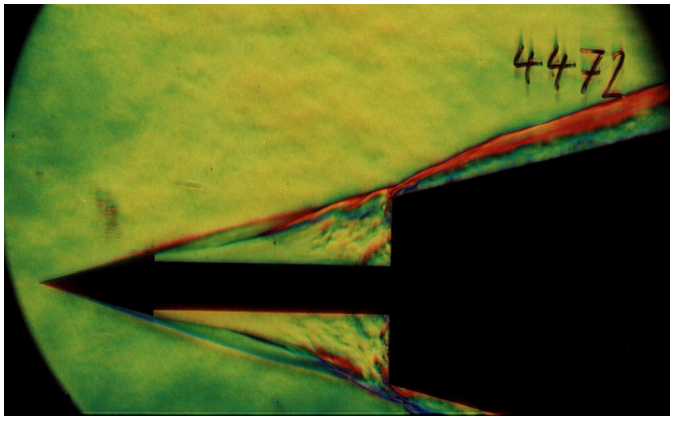
4.3 Assessment of flow unsteadiness and axisymmetry

The various flow photographs, shown in this section, indicate a good correlation of the larger scale motions around the model. Departure from axisymmetry – temporally – is only obvious at the smaller scale motion in these photographs. Figures 17, 18, 19 and 20 show measured pressure time-histories on the cavity back face, for cavities 3, 2, 1 and 12, using the transducer locations specified in Table 2. In each case the two traces represent sensors separated by 180 degrees in azimuth – that is on opposite sides of the model. These use the largest tapping size shown in the frequency response assessment of Fig. 3, and are regarded as adequate to resolve the larger scale, lower frequency fluctuations, essentially those arising from motions on the scale of the overall cavity size. The time scale is normalised by edge velocity and cavity length (100mm for cavity 12 and 50mm for the others). In each case one of the two traces includes the discrete sampling values; these were acquired at 125kHz.

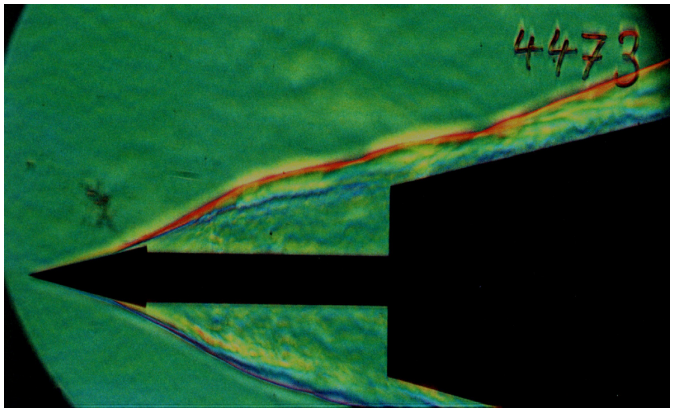
For cavities 1 and 12, the vigorous oscillatory motion seen in the visualisation is reflected in the high amplitude fluctuations of the experimental pressure time-histories of Figs 19 and 20. Both cases show a clear periodic signal, with amplitude modulation. Cavity 12 is twice the length of cavity 1, but using the normalised time TU_E/L_C provides virtually identical cycle times of $\Delta TU_E/L_C$ = 6·0 for cavity 1 and 5·8 for cavity 12 (taken from longer records than those shown here). The comparable values from CFD, in the case of cavity 1 as shown in the CFD of Fig. 7, are 5·75 and 5·7 respectively. There is also a good match between pressure-histories on opposite sides of the cavity, indicating a good axisymmetry for this larger scale motion. The departure from this matching is for the higher frequency events, that are less likely to be correlated across the cavity. It is also notable that the higher frequency events, and the variation in range of the extreme values, is much more pronounced for the positive-going fluctuations rather than negative-going.

For cavities 2 and 3, where the motion has been referred to as 'slightly unsteady', the signal amplitude is less (it is recognised that amplitude clearly depends upon position on the cavity wall), and the frequency is clearly higher, than for cavities 1 and 12. This indicates motions associated with the development of 'local' disturbances in the shear layer and there is an absence of the recognisable low frequency oscillations seen for cavities 1 and 12. CFD for cavities 2 and 3 give fluctuation levels much lower than those of the experiment. The higher frequency disturbances for cavities 2 and 3 must also be poorly correlated across the cavity (diameter). A simplistic

https://doi.org/10.1017/S0001924000004851 Published online by Cambridge University Press



(a)



(b)

Figure 16. Schlieren images for the cavity 12 case.

model of the acoustic communication paths within the cavity explain why. The direct paths, W_f and W_b, across the cavity front-face and back-face respectively, are

$$W_f = 2L_F \mathrm{Sin}(\delta); W_b = 2(L_F + L_C)\mathrm{Sin}(\delta) \quad \ldots (4)$$

where δ is the cone semi-vertex angle of 15 degrees.

The times, $T_{ac,f}$ and $T_{ac,b}$, for acoustic waves with a mean sound speed, $\bar{a}$, to traverse the front- and back-face are;

$$T_{ac,f} \approx \frac{W_f}{\bar{a}}; T_{ac,b} \approx \frac{W_b}{\bar{a}} \quad \ldots (5)$$

From Table 3. the edge velocity U_e is $0{\cdot}956U_\infty$ or $8{\cdot}51a_\infty$. Thus the normalised times for these wave transits are then

$$\frac{T_{ac,f}U_E}{L_C} \approx 17{\cdot}02\frac{a_\infty}{\bar{a}}\frac{L_F}{L_C}\mathrm{Sin}(\delta) \quad \ldots (6)$$

$$\frac{T_{ac,b}U_E}{L_C} \approx 17{\cdot}02\frac{a_\infty}{\bar{a}}\left(1+\frac{L_F}{L_C}\right)\mathrm{Sin}(\delta) \quad \ldots (7)$$

From CFD the maximum temperature in the cavity is about ten times the free stream value, and the maximum speed of sound is therefore approximately $3{\cdot}2a_\infty$, which is then used for a. Table 4. provides tabulated values of $T_{ac,f}U_E/L_C$ and $T_{ac,b}U_E/L_C$ for the various cavity cases. These are likely to be lower bounds on the transit times, since the estimate for a is high. For motion to be well correlated across opposite sides of the cavity requires the transit time to be small compared with the time scales for the axial motions. This is not the case for cavities 2

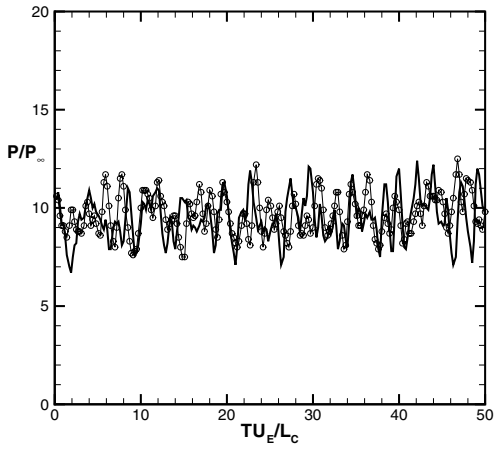


Figure 17. Experimental pressure time-histories for cavity 3 on the back-face of the cavity, with two pressure tappings separated by 180 degrees in azimuth at the location given in Table 2. The tapping diameter 2·5mm corresponds to the largest shown in Fig. 3. The two histories are indicated, respectively, by a thick line and by a thin line-plus-symbol.

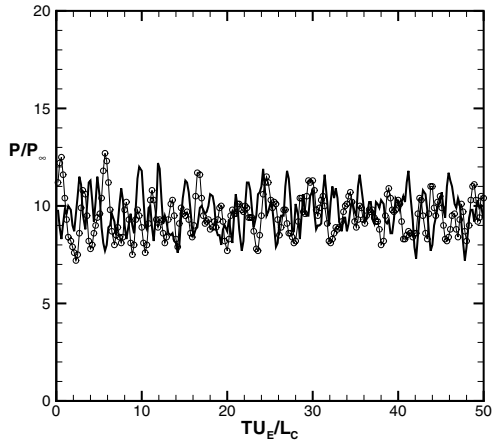


Figure 18. Experimental pressure time-histories for the cavity 2 on the back-face of the cavity. Other detail as in Fig. 17.

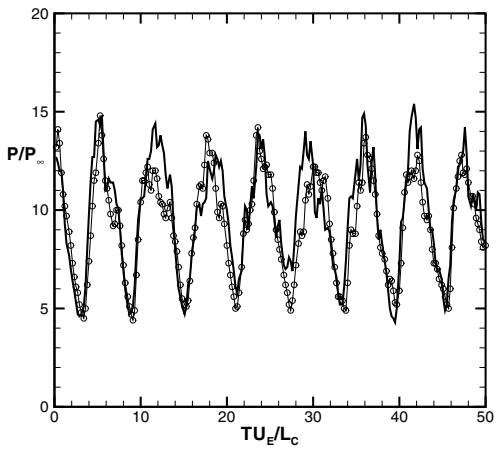


Figure 19. Experimental pressure time-histories for the cavity 1 on the back-face of the cavity. Other detail as in Fig. 17.

https://doi.org/10.1017/S0001924000004851 Published online by Cambridge University Press

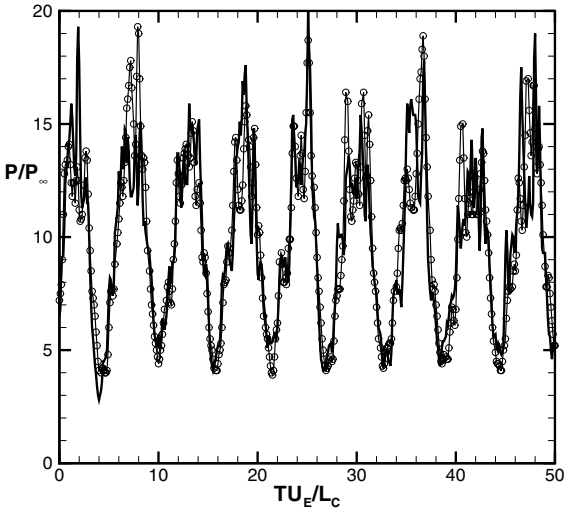


Figure 20. Experimental pressure time-histories for the cavity 12 on the back-face of the cavity. Other detail as in Fig. 19.

Table 4
Estimate of shortest time for the transit of acoustic waves across the front- and back-faces of the cavity

cavity	L_F/L_C	$T_{ac,f}U_E/L_C$	$T_{ac,b}U_E/L_C$
12	0·5	0·69	2·06
1	1·0	1·38	2·75
2	2·0	2·75	4·13
3	3·0	4·13	5·51

and 3, but should become increasingly more so for the longer time scales associated with the large amplitude, whole-cavity motion of cavities 1 and 12. Indeed, in the latter cases, Figs 19 and 20. show that the long timescale motion matches very well between the transducer pair, but that the superimposed high frequency 'spikes' are poorly correlated.

5.0 TRANSITION BETWEEN HIGHLY UNSTEADY FLOW AND STEADY OR 'MILDLY UNSTEADY' FLOW

The schlieren photographs show that there are some cases where the amplitude of shear layer motion is small, whilst other cases show very significant amplitudes, with separation moving intermittently onto the fore-body and with a very evident fluctuation of the bow shock wave as well. The bow shock wave introduces an extra element to the feedback cycle, provided that the cavity length is sufficiently long, since it is possible for disturbances at the upstream separation position (either the cavity lip or on the fore-body) to transmit out to the bow shock wave and reflect back to the cavity. If the reflected wave returns downstream of the rear cavity lip then it can have no influence. If it reflects directly onto the free shear layer it potentially can contribute to the feedback mechanism. The limiting case for the longest cavity that could avoid this interaction is simply for the radiation of a Mach wave from the upstream lip of the cavity and its subsequent reflection back from the shock wave to the downstream lip. This is given by

$$\frac{L_C}{L_F} \approx 2\left(\frac{\mathrm{Tan}(\theta-\delta)}{\mathrm{Tan}(\mu)-\mathrm{Tan}(\theta-\delta)}\right) \quad \ldots (8)$$

where δ is the cone angle (15 degrees), θ is the apex shock wave angle relative to the free stream and μ is the average Mach angle in the shock layer. For hypersonic thin shock layer flows this value is very close to the computed boundary-layer edge value and provides a value $L_c/L_f \cong 0{\cdot}73$. A larger value of L_c/L_f would provide the possibility for this interaction mechanism to occur. Given that finite strength shock waves are inclined more steeply to the flow than Mach waves, and that the separation position can move upstream of the forward cavity lip onto the fore-body, the critical ratio is likely to be less than the value above.

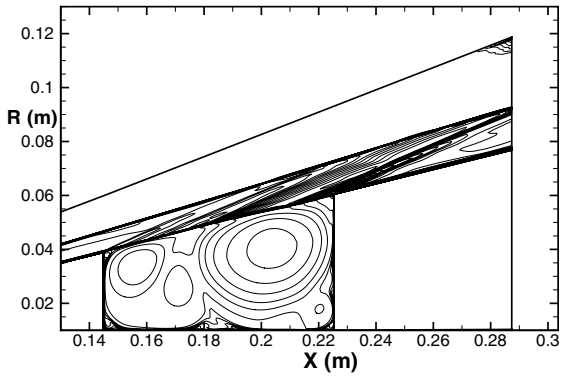
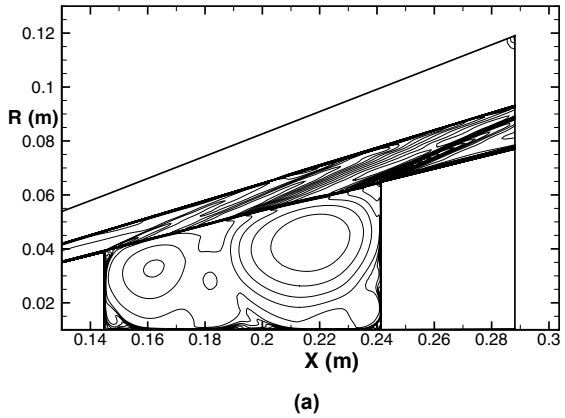


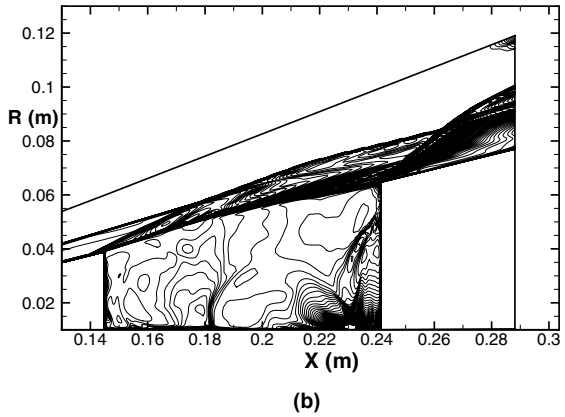
Figure 21. CFD for fore-body wetted length of 150mm and $L_c/L_f = 0{\cdot}556$.

CFD and experiment have been used extensively to identify the domain for 'weakly' oscillating and 'strongly' oscillating flows. The first point, specifically identified from the CFD and supported by the experimental data, is that the highly oscillatory flow corresponds to large scale periodic shedding of vortical fluid from the downstream end of the cavity with the separation position clearly moving (unsteadily) upstream onto the fore-body. This generation of sufficiently large pressures in the cavity to propel the separation position forwards, onto the fore-body, appears to be an important element in the transition to highly unsteady flow; this may be specific to this study, but there does appear to be no observations on this mechanism from other works in the literature. Figure 21 shows a CFD simulation for the 150mm fore-body with a cavity length of 83·3mm, giving a ratio for L_c/L_f of 0·556. In this instance the CFD was impulsively started and after several ms. of transients the motion subsided to a 'slightly' unsteady motion with separation fixed at, or very close to, the upstream lip of the cavity. Next Fig. 22 shows the CFD simulation for the same fore-body but with the cavity extended to 100mm, that is corresponding to cavity 34 with $L_c/L_f = 0{\cdot}667$. Two simulations are shown in this figure, one (Fig. 22(a)) started from a near-steady state (using a 'stretched' output from Fig. 21 mapped onto the new cavity geometry) and one (Fig. 22(b)) produced from an impulsive start. These now produce two separate limit states in contrast to the shorter cavity length of Fig. 21. Figure 22(a) maintains a clear vortex system within the cavity, with separation fixed at the upstream cavity lip and reattachment oscillating slightly about the downstream lip in response to small movements of the vortex system. Figure 22(b) is just one 'snapshot' within the shedding cycle, but still shows that in this case the motion is highly unsteady, with the separation position moving intermittently onto the fore-body, as shown in Figure 23. This was also noted in Fig. 12. The corresponding schlieren visualisation of Fig. 14, interestingly, indicates only mild unsteadiness, comparable to Fig. 22(a) rather than Fig. 22(b). This probably indicates that although the gun tunnel is an impulsive facility, the actual flow startup times are still large compared with the time scales associated with the cavity flow. Figure 24 shows a further extension of the cavity length to give $L_c/L = 0{\cdot}8$, again providing both a near-steady solution and also a highly oscillatory state as alternatives. Again, the pictures for the oscillatory state are simply individual snapshots and the flow pattern will vary significantly through the cycle. Despite very long computational runs these cases maintained the two possible flow outcomes. Figure 25

https://doi.org/10.1017/S0001924000004851 Published online by Cambridge University Press



(a)



(b)

Figure 22. CFD for fore-body wetted length of 150mm and L_c/L_f = 0·667, that is cavity case 34. (a) simulation started from an initial near-steady state and (b) impulsive start to simulation.

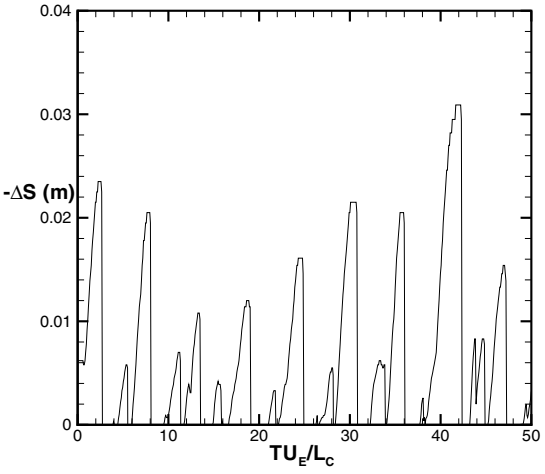
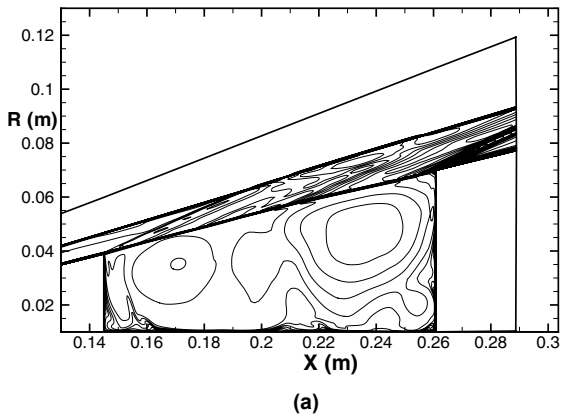
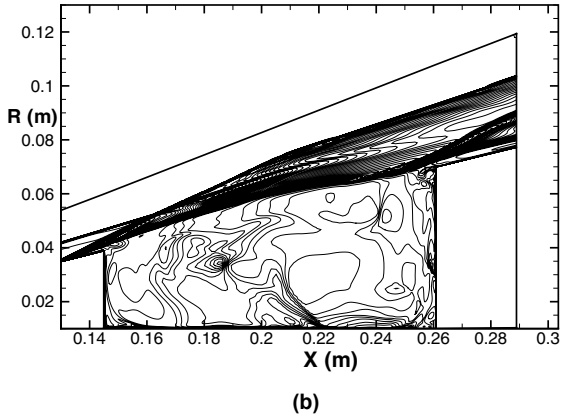


Figure 23. CFD modelling for the movement of separation position, with time, on the fore-body corresponding to the case of Fig. 22(b).

models the same fore-body length, but with a further lengthened cavity to give L_c/L_f = 0·962. In this case the simulation was started with a near-steady solution but, after a long time (10ms), the flow eventually established as a highly oscillatory motion so that only the one limit state was apparently possible.



(a)



(b)

Figure 24. CFD for fore-body wetted length of 150mm and L_c/L_f = 0·8. (a) simulation started from an initial near-steady state and (b) impulsive start to simulation.

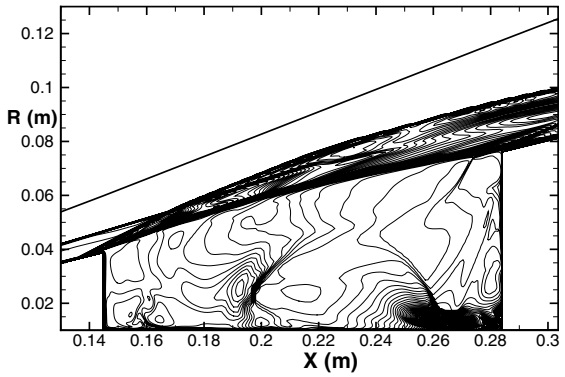
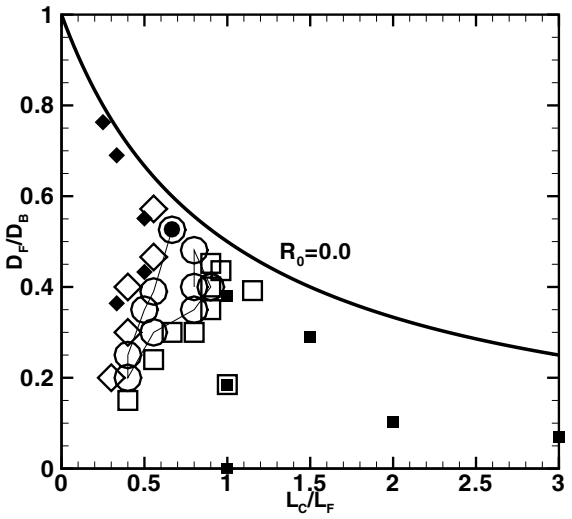


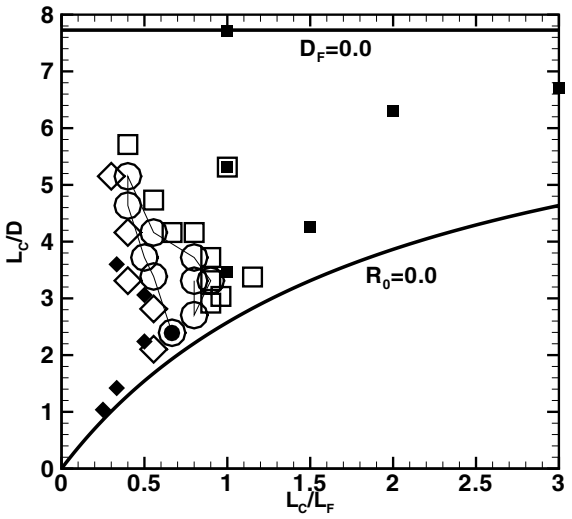
Figure 25. CFD for fore-body wetted length of 150mm and L_c/L_f = 0·962. The simulation was started from steady-state.

These simulations have been continued for a range of cases, changing both the ratio L_c/L_f and also changing the centre-body radius R_O. Figure 26 . shows the ensemble of flow states in the plane L_c/L_f *versus* both D_f/D_b and also L_c/D. The limit boundary of zero centre-body (R_O) thickness is shown, together with the maximum centre-body thickness (D_F= 0, *x*-axis for Fig. 26(a)). The CFD data identify points as 'slightly' oscillatory (separation not moving forwards onto the fore-body), strong oscillation (separation moving forwards onto the fore-body) and 'dual' case where both options are possible depending upon

https://doi.org/10.1017/S0001924000004851 Published online by Cambridge University Press



(a)



(b)

Figure 26. Composite presentation of the CFD simulations (open symbols) and experimental cases (solid symbols) in the domain of L_c/L_f versus (a) D_F/D_B and (b) L_c/D. Diamonds, circles and squares represent weak oscillation, 'transitional or dual-state' and strong oscillation respectively.

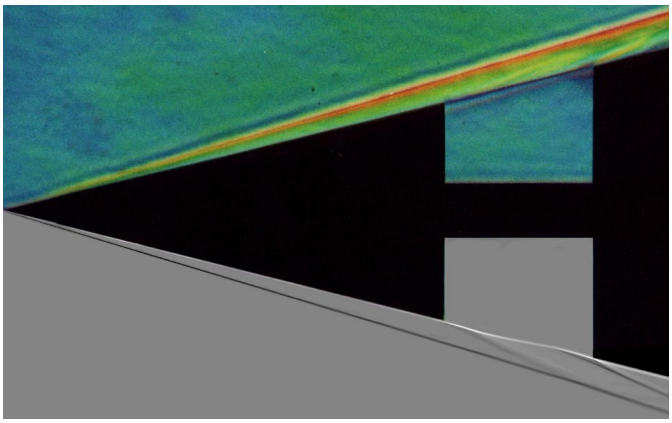


Figure 27. Cavity 3 (L_f/L_c = 3) composite schlieren image. The upper half shows the experimental schlieren image and the lower the CFD image.

how the simulation is started. The Fig.also includes the database of results collected from the experimental model, though precise identification of state (with a single photograph per run) is not always easy. Figure 26 shows that a value of 0·73 for L_C/L_F is indeed very close to the threshold beyond which a strongly unsteady flow will always occur. As the centre-body radius R_O is increased, and the depth of the cavity front face D_F therefore tends to zero, then the strongly oscillatory flow is found to occur for lower values of L_C/L_F; these are cases where the separation front penetrates significantly forwards onto the fore-body, so that the separation-shock/apex-shock interaction can still produce a wave reflection that impinges onto the free shear layer.

The Mach 8 study by Bellone and Stollery[25] presents a ratio for L_C/L_F of 0·43. For Mach 8·0 flow, past a 10 degrees semi-angle cone, the shock wave angle θ and the average shock layer Mach angle are 13 degrees and 10·25 degrees respectively. According to Equation (8) the critical value for L_C/L_F would be approximately 0·82. The fact that this is substantially greater than the experimental value is consistent with the observation that the cavity flow was only mildly unsteady.

6.0 FURTHER COMMENTS ON THE FLOW PHYSICS

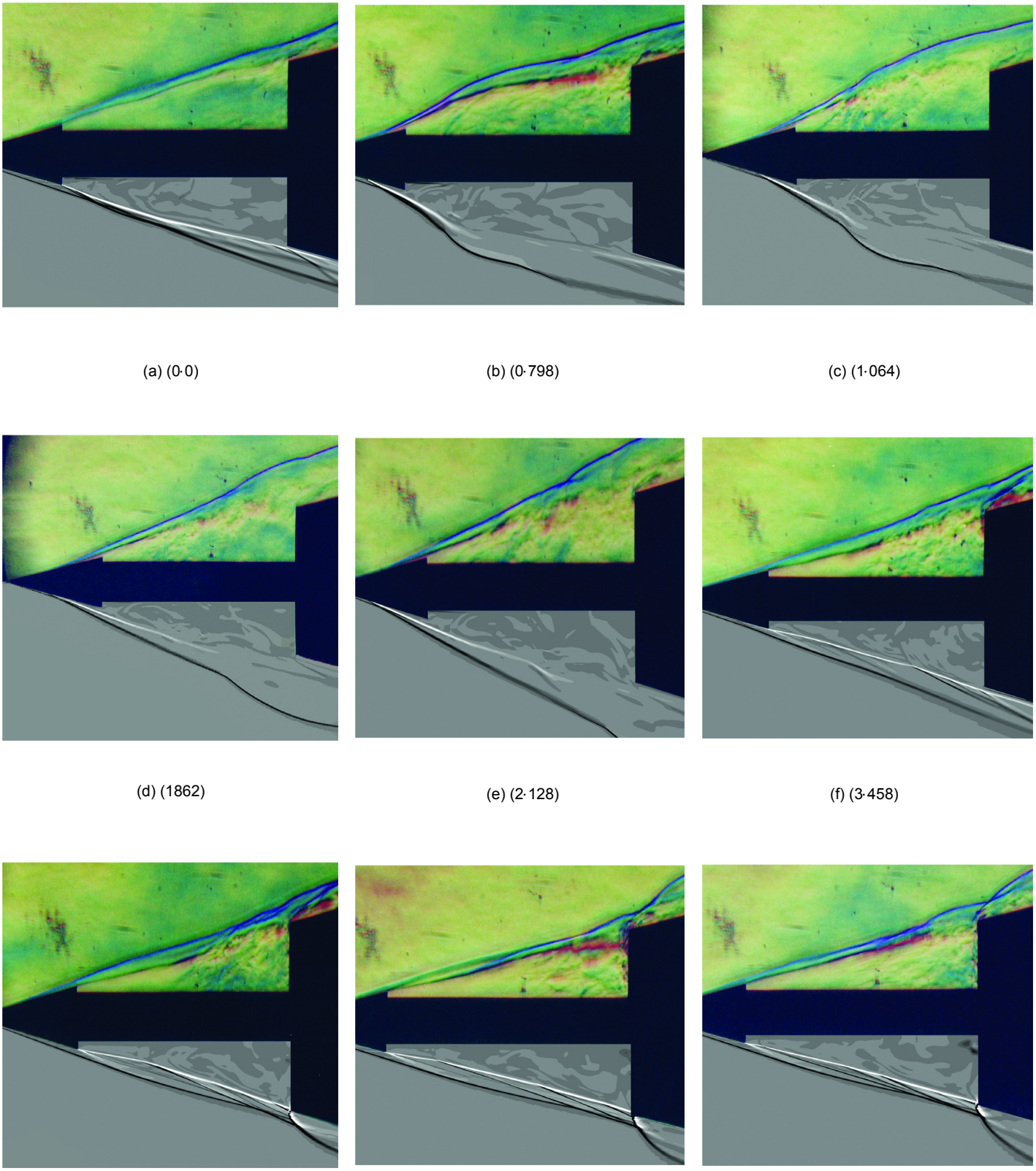
Although we refer to the flows as cavity flows, they are not cavities within a strict definition. For the highly oscillatory cases the movement of the separation point from the forward lip onto the fore-body is an important element in the process and these flows could be considered to resemble 'spiked bodies' (see, for example, Feszty, Badcock and Richards[34]). Such a perception is only too obvious when Fig. 28. for cavity 12 is considered, for example. In turn, the weakly oscillating cases differ geometrically from some aspects of the 'classical' 2D planar cavity. It is unclear, for example, how significant the obstructive effect of the cavity floor is. Figure 26 contains two limit lines for the sting. The case $R_O = 0$ is easy enough to achieve computationally and cavity 4 in Fig. 11 shows how modest the obstruction to transverse motions in the cavity can be.

The main significance of Fig. 26 is that it categorises cavity cases in terms of the severity of their unsteady motion. Here we expand upon some specific cases: Cavity 3 and 2 ('steady' or 'mildly unsteady'), cavity 1 and 12 ('highly unsteady').

6.1 Cavity 3 (L_C/L_f = 0·333, D_F/D_B = 0·69) and Cavity 2 (L_C/L_F = 0·5, D_F/D_B = 0·551)

For these cases the experiments show low amplitude oscillations. The CFD predictions indicate much lower levels, but both are in agreement that these cases are 'nearly steady' and that separation does not (or hardly ever) moves onto the fore-body. Schlieren photographs for cavities 2 and 3 were shown earlier in Fig. 11 and a composite schlieren/CFD comparison for cavity 3 is made in Fig. 27. The timescale for the fluctuations for cavities 2 and 3, judging from Figs 17 and 18, are in the range $1 \leq TU_F/L_C \leq 2$. This is probably an overestimate, because of the transducer/tapping filtering effect, and it is almost certainly too short a timescale to correspond to any longitudinal feedback process, where vortex convection along the shear layer from the forwards cavity lip leads to a return reflected pressure wave from the cavity back-face. The poor correlation – essentially random correlation – of these fluctuations across the cavity (diameter) has already been noted. That CFD should underpredict the magnitude of experimental fluctuations is a surprise, given the earlier comments about inevitable filtering effect of the experimental frequency resolution, and the CFD appears to be missing out on some aspect of the flow. Limited CFD attempts to provoke Kelvin-Helmhotz instability were not successful. There are insufficient data to comment on whether the fluctuations represent early stages of transition. Almost certainly transient 3D effects must be important. The very lack of correlation across the cavity shows that they must occur and the cavities such as 34 show 3D features in the shear layer; the work by Jackson *et al*[24] for

https://doi.org/10.1017/S0001924000004851 Published online by Cambridge University Press



(a) (0·0) (b) (0·798) (c) (1·064)

(d) (1862) (e) (2·128) (f) (3·458)

(g) (4·522) (h) (4·788) (i) (5·054)

Figure 28. Schlieren comparison with CFD images for the cavity 12 geometry. Each sub-figure shows the experimental image on the upper half and the numerical on the lower. The dimensionless time TU_E/L_C (in parentheses) shows when the numerical image was captured, with the start of the cycle set arbitrarily to zero.

https://doi.org/10.1017/S0001924000004851 Published online by Cambridge University Press

a highly axisymmetric (in the mean) laminar cavity flow suggested that 3D Gortler-vortex structures might be present within the cavity flow. Linked with this is also the suspicion, but without support, that an ingredient of the experimental oscillation is the shedding of shear layer disturbances from the forward cavity lip in response to slight movement of the trapped vortex systems in the cavity interior.

6.2 Cavity 1 (L_C/L_F = 1·0, D_F/D_B = 0·185) and Cavity 12 (L_C/L_F = 2·0, D_F/D_B = 0·102)

These shows significant unsteadiness. The time-sequence of Fig. 13, for cavity 1, and Fig. 28 for cavity 12, show 'one cycle' of motion, as determined from the CFD, compared with schlieren photographs selected from a large number. The larger scale motions do appear to be well correlated across the cavity (diameter), producing a good flow axisymmetry, consistent with the basic oscillation time scales being reasonably large compared with the transverse acoustic wave propagation times. The smaller scale events superimposed upon the shear layer, by the same argument should not be – and are not – well correlated. The CFD reproduces well the fundamental oscillation frequency, shown by comparison of Figs 7 and 19. That it over-predicts rms pressure values, or the extreme fluctuation levels, is almost certainly the filtering effect of the experimental transducer/tapping arrangement. The narrow band spikes, shown in the CFD, that contribute in large part to this discrepancy are at such a high frequency that any experimental counterpart could not, in fact, be axisymmetric. Further work is actually required, using three-dimensional simulations and enhanced frequency resolution experimentally, to resolve this issue.

An intrinsic feature of these cases is the interaction between the bow shock wave and the unsteady cavity motion. The CFD modelling of movement of the separation position, seen for example in Fig. 12, appears to be consistent with experiment. What the experiments cannot investigate, being limited to a single photograph per run, is the 'slow growth' and 'rapid collapse', in time, of the front as predicted by CFD.

7.0 CONCLUDING REMARKS

The use of laminar axisymmetric CFD appears generally to be justified by the results. Probably the most important departure from this, from the CFD modelling viewpoint, would be the inclusion of three-dimensionality. At the experimental level is is clear that enhanced frequency resolution would resolve some of the issues in the disparity between CFD and experiment. Flow visualisation has been shown to be important. An ideal would be high speed filming since the 'cycle sequence' in the experiments was constructed, quite plausibly, from inspection of the CFD but it would be desirable to generate these independently. They could then further be matched with synchronised pressure time-history records.

This work was funded by EPSRC studentship and this support is gratefully acknowledged. Our thanks are also due to Mr Roland Hutchins and Mr Steven Johnson for their excellent craftsmanship in the model and instrumentation manufacture and for operation of the gun tunnel. We also thank Dr Neil Murray who provided critical assistance in the experiments.

REFERENCES

1. KRISHNAMURTY. K. Acoustic radiation from two-dimensional rectangular cutouts in aerodynamic surfaces, NACA TM 3487, August 1955.
2. CHARWAT, A.F., ROOS, J.N., DEWEY, F.C. and HITZ, J.N. An Investigation of separated flows, *J Aero Sci*, 1961, **28**, (6).
3. ROSSITER, B. Wind Tunnel Measurements on the flow over rectangular cavities at subsonic and Transonic speeds, Ministry of Aviation, Aeronautical research council, London, 1966.
4. HELLER, H.H. and BLISS, D.B. The Physical mechanisms of Flow-Induced Pressure Fluctuations in Cavities and concepts for their suppression , AIAA Paper-1975-471, 1975.
5. NICOLL, K.M. A Study of laminar hypersonic cavity flows, 1964, *AIAA J*, **2**, (9), 1535-1541.
6. HAHN, M. Experimental investigation of separated flow over a cavity at hypersonic speed , AIAA Paper 68-672. 1968.
7. SAROHIA, V. Experimental investigation of oscillations in flows over shallow cavities, *AIAA J, 1976*, **15**, 7, 984-991.
8. ROCKWELL, D. and KINSELY, C. The organized nature of flow impingement upon a corner, *J Fluid Mech*, 1979, **93**, Part 3, 413-432.
9. NESTLER, D.E. Heat transfer to steps and cavities in hypersonic turbulent flow, *AIAA J*, July 1969, **7**, (7).
10. NESTLER, D.E. An experimental study of hypersonic cavity flow, *J Spacecraft and Rockets*, June 1982, **19**, (3).
11. ROCKWELL, D. and NAUDASCHER, E. Review – Self-Sustaining Oscillations of flows past cavities, *J Fluid Mech,* 1978, **100**, pp 152-165.
12. HANKEY, W.L. and SHANG, J.S. Analyses of pressure oscillations in an open cavity, *AIAA J*, 1980, **18**, (8), pp 892-898.
13. DUSING, D.W., FOX, C.W., TAM, C., ORKWIS, P.D. and DISIMILE, P.J. An experimental and computational study of unsteady supersonic 2-D open cavity flow physics, 1994, AIAA Paper 94-0528.
14. ORKWIS, P.D. and DISIMILE, P.J. The effect of yaw angle on the dominant frequencies of rectangular cavities in supersonic flow , Rept. 96-010, Dept of Aerospace Engineering and Engineering Mechanics, University of Cincinnati, OH, USA, 1996.
15. TAM, C., ORKWIS, P.D. and DISIMILE, P.J. Comparison of Baldwin-Lomax turbulence models for two-dimensional open cavity computations, *AIAA J*, 1996, **34**, (3), pp 629-631.
16. TAM, C., ORKWIS, P.D. and DISIMILE, P.J. Algebraic turbulence model simulations of supersonic open-cavity flow physics, *AIAA J*, 1996, **34**, (11), pp 2255-2260.
17. MORGENSTERN, A. and CHOKANI, N. Computation of hypersonic open cavity flows, AIAA Paper 93-2969, 1993.
18. MORGENSTERN, A. and CHOKANI, N. Computation of hypersonic flow over three-dimensional cavity, AIAA Paper 94-0631, 1993.
19. MORGENSTERN, A. and CHOKANI, N. Prediction of hypersonic cavity flow dynamics, AIAA Paper 99-0171, 1999.
20. COLONIUS, T., BASU, A.J. and ROWLEY, C.W. Numerical investigation of flow past a cavity, AIAA Paper 99-1912, 1999.
21. STURGESS, G.J. and HSU, K-Y. Entrainment of mainstream flow in a trapped-vortex combustor, AIAA Paper 97-0261, 1997.
22. BOWERSOX, R.D.W. and DAVIS, D.L. Computational fluid dynamics analysis of cavity flame holders for scramjets, 1997, AIAA Paper 97-3270.
23. EDWARDS, J.A., RONA, A. and ZHANG, X. The effect of trailing edge geometry on cavity flow oscillation and pressure feedback, *Aeronaut J*, 1998, **102**, (1013), pp 129-136.
24. JACKSON, A.P., HILLIER, R. and SOLTANI, S. Experimental and computational study of laminar cavity flows at hypersonic speeds, *J Fluid Mech*, 2001, **427**, pp 329-358.
25. BELLONE, F. and STOLLERY, J.L. Cone cavity flow at M = 8·2 with injection of air and helium, *Aeronaut J*, 1999, **103**, (1029), pp 529-535.
26. COOK, W.J. and FELDERMAN, E.J. Reduction of data from thin-film heat-transfer gauges: a concise numerical technique, *AIAA J*, 1966, **4**,(4), pp 561-562.
27. SCHULTZ, D.L. and JONES, T.V. Heat-transfer measurements in short--duration hypersonic facilities, AGARDograph, **165** , 1973.
28. HILLIER, R., KIRK, D. and SOLTANI, S. Navier-Stokes computations of hypersonic flows, *Int J Num Meth Heat and Fluid Flow*, 1995, **5**, pp 195-211.
29. BEN-ARTZI, M. and FALCOVITZ, J. A second-order Godunov-type scheme for compressible fluid dynamics, *J Comp Phys,* 1984, **55**, pp 1-32.
30. KEYES, F.G. The heat conductivity, viscosity, specific heat and Prandtl numbers for thirteen gases, Massachusetts Institute of Technology, USA, Project Squid, Tech Report 37, 1952.
31. ZANCHETTA, M.A. and HILLIER, R. Blunt Cone Transition At Hypersonic Speeds: The Transition Reversal Regime, In Transitional Boundary Layers in Aeronautics. HENKES, R.A.W.M. AND VAN INGEN, J.L. (Eds), North-Holland. 1996.
32. MALLINSON, S.G., JACKSON, A.P., HILLIER, R., KIRK, D.C., SOLTANI, S. and ZANCHETTA, M. Gun tunnel flow calibration: defining input conditions for hypersonic flow computations, Shock Waves, 2000, **10**, pp 313-322.
33. FERNHOLZ, H.H. and FINLEY, P.J. A critical compilation of compressible turbulent boundary layer data, AGARDograph 223, 1977.
34. FESZTY, D., BADCOCK, K.J. and RICHARDS, B.E. Utilising CFD in the investigation of high-speed unsteady spiked body flows, *The Aeronaut J*, 2002, pp 161-174.

https://doi.org/10.1017/S0001924000004851 Published online by Cambridge University Press